Geoscientific process monitoring with positron emission tomography (GeoPET)

Johannes Kulenkampff, Marion Gründig, Abdelhamid Zakhnini, Johanna Lippmann-Pipke

Institute of Resource Ecology, Helmholtz-Zentrum Dresden-Rossendorf, Germany

5 *Correspondence to*: J. Kulenkampff (j.kulenkampff@hzdr.de)

Abstract. Transport processes in geomaterials can be observed with input-output experiments, which yield no direct information on the impact of heterogeneities, or they can be assessed by model simulations based on structural imaging with µCT. Positron emission tomography (PET) provides an alternative experimental observation method which directly and quantitatively yields the spatiotemporal distribution of tracer concentration. Process observation with PET benefits from its

10 extremely high sensitivity together with a resolution that is acceptable in relation to standard drill core sizes. We strongly recommend applying high-resolution PET scanners in order to achieve a resolution in the order of 1 mm.

We discuss the particularities of PET applications in geoscientific experiments (GeoPET), which essentially are due to high material density. Although PET is rather insensitive to matrix effects, mass attenuation and Compton scattering have to be corrected thoroughly in order to derive quantitative values.

15 Examples of process monitoring of advection and diffusion processes with GeoPET are illustrating the procedure and the experimental conditions, as well as the benefits and limits of the method.

Keywords: Process tomography, positron emission tomography, PET, transport experiments, tracer, heterogeneity

1 Introduction

1.1 Aims

It is common practise to observe and quantify transport in geological materials with input-output experiments which treat the material as black box. However, these methods miss heterogeneous effects, like preferential transport, and also are

5 disadvantageous when the process is slow, or when an applied tracer is retained by internal reactions. One approach for unravelling transport processes in geological materials is a most detailed description of the structure and composition of the matrix and the pore space. These provide boundary conditions for model simulations whose final results are compared and validated with input-output experiments. Such model simulations require specific geochemical parameters for the tracer species and the particular material, which are derived from other experiments.

10 Direct observation of the propagating species during the course of the process is a complementary approach which yields more intrinsic information on the process. Such process-tomographic methods are particularly suited when complexity or fineness impede the compilation of an applicable structural model.

Positron emission tomography (PET) is originally a nuclear medical method which takes advantage from the simple but most sensitive detectability of radiotracers. Successfully, we strive to broaden the scope of PET-applications to geoscientific and

15 technical use since more than 15 years. The potential of the method was proven and communicated as an important experimental method for enhanced understanding of geochemical processes in soils and rock formations, for modelling and upscaling.

1.2 Process tomography modalities

Geological materials are generally heterogeneous with respect to structure and composition. Moreover, the internal structure

20 is highly complex, with contributions from hierarchical scaling (fractal behaviour) and non-scaling contributions on a particular scale. On larger scales this behaviour is considered by anticipating a representative elementary volume that is supposed to combine all heterogeneities in a homogeneous parameter set. Disregarding tomographic methods, the characteristic size of this volume had to be derived from laboratory experiments on a large number of differently sized samples. Structural tomographic methods, like μCT, now allow characterizing the structure comprehensively and over a

25 large scale. Then, model simulations can be conducted on these structures, taking into consideration the parameters of the particular process. However, the huge size of hierarchical tomographic data currently precludes composition and processing of pore-scale simulation models in detailed structures. Currently, typical model simulations are conducted on structural models that are based on the limited resolution range of a particular tomographic method.

This type of bottom-up approach could miss significant features of transport processes, because the chemical species are

30 progressing in a highly heterogeneous material with disorder from the molecular to the centimetre scale. Often, preferential transport and reactions at distinct sites of the internal surface have to be considered, with major contributions from structures

below the resolution of the tomographic modality. These limitations with respect to transport processes could be overcome by direct tomographic observation of the transport processes.

The number of applications of industrial process tomography is rapidly growing. Industrial process tomography means observation of a large variety of processes by spatiotemporal monitoring of process parameters for process understanding and control (Wang, 2015; Williams and Beck, 1995). Applications of these methods are also growing in geosciences; some of these methods were even originally developed for geoscientific purposes, like electrical resistivity tomography.

The tomographic observation of substances in disjoint phases is possible with a large number of imaging modalities which respond to specific properties of the phases, like CT (density) and ultrasonic imaging (elastic velocity), but they rely on significant contrast. CT-data are commonly processed in order to produce structural images, segmenting the greylevel images into two or multiple domains with different density. Therefore, the most significant characteristics are spatial resolution and homogeneity of the mapping, in order to facilitate segmentation.

A major class of processes in the geosphere are transport phenomena, including advection, dispersion, and molecular diffusion of dissolved substances or particles. Frequently, the most meaningful observable is the concentration of dissolved or dispersed species, which is an intensive thermodynamic parameter that is most relevant for aligning observations with simulation results from models of the processes. Concentration is a continuous value, referred to a finite test volume which is defined by the spatial resolution of the measuring method. Here, spatial resolution is merely the response function which controls the smoothing of the image.

Ionic concentrations can be monitored with different types of Electrical Impedance Tomography (EIT). These are frequently applied to investigate transport processes of conductive solutions in soils and rocks. However, electrical resistivity, as one of these parameters, depends on a variety of material parameters and rock-fluid interactions; therefore the result is not univocal. Other imaging methods apply tracers for labelling, which facilitates detection and quantification of the species (Hevesy and Paneth, 1913; Garrett, 1963). Spatiotemporal visualization of labelled substances requires tomographic methods with selective response to the tracer. In the field of biomedical research these techniques are called "molecular imaging methods" (Weissleder, 2010). From these methods, magnetic resonance imaging (MRI), single photon emission computed tomography (SPECT), and positron emission tomography (PET) are suited for opaque media. In contrast to ERT, these methods selectively respond to the concentration of protons or specific tracer isotopes, respectively, but they are mere laboratory applications and barely suitable for field applications. The methods differ with regard to the matrix effect. In the case of MRI, distortions of the magnetic field by paramagnetic compounds of the matrix, and in the case of SPECT, radiation attenuation and scattering, are constricting their applicability. PET is least affected by material inferences.

PET is perfectly selective and by far the most sensitive method, because the response is directly and only related to the number of decaying positrons, and thus the number of tracer atoms. Depending on the source distribution, it requires only a small number of events (in the order of 100 per voxel) to reconstruct the tomogram. A typical voxel size around 1 mm means a cube of water containing about 10^{19} atoms. This means, the sensitivity is better than pico-moles per μL, depending on the

decay characteristics of the PET-nuclide and the noise level. With this ultimate sensitivity, PET can serve as "gold-standard" for tomographic imaging of tracer concentrations. Its spatial resolution of 1 µL is appropriate for typical sample sizes of 1 L. Currently, structural imaging with µCT brings a great increase of the understanding of transport processes in geomaterials. The geometry of the pore space from segmented µCT-images provides realistic boundary conditions for model simulations.

5 Commonly, the results of such simulations are verified with rather simple input-output experiments on macroscopic samples that only consider the integral response to an input signal. Instead, we promote the application of process observation with PET for directly quantifying mass transport inside the sample.

PET is a particularly suitable method when mass transport through argillaceous rocks is dominated by the small sizes of the pores, which complicate the creation of a realistic model. Methods with very high spatial resolution, like FIB-SEM or nano-

10 CT are able to visualize the pore structure in the nanometre range, but they are applicable only on millimetre-sized samples. Hence, these are not suited to consider structures on the millimetre range, like fine layering and other heterogeneities. Furthermore, N_2 adsorption porosimetry (e.g. Nagra (2002)) suggests that a significant portion of the pores falls below the resolution of even highest resolving imaging methods. This means that connecting pores are not segmented and therefore excluded from the structural model. Here, PET is a dependable method for monitoring the propagation of the tracer through

15 the fine-grained material, although its spatial resolution is far beyond the largest pore structures.

1.3 GeoPET: Applications of PET in geosciences

A large amount of comprehensive literature exists on medical PET (Wernick and Aarsvold, 2004; Bendriem and Townsend, 1998; Phelps, 2006). Here we summarize the principal functional principle with emphasis on geoscientific applications. Other non-medical applications (Benton and Parker, 1996; Hawkesworth and Parker, 1995; Hawkesworth et al., 1991;

20 Parker et al., 1993; Parker et al., 2002; Parker et al., 1994; Stein et al., 1997) are addressing similar issues.

Already shortly after the introduction of clinical PET scanners, which were based upon the work of Phelps and Ter-Pogossian (Ter-Pogossian et al., 1975), first geoscientific studies were conducted with PET. Numerous investigations of flow processes in various rock formations were conducted since 1989 (van den Bergen, 1989; Benton and Parker, 1996; Khalili et al., 1998; Degueldre et al., 1996; Ogilvie et al., 2001; Tenchine and Gouze, 2005; Goethals et al., 2009; Kinsella et

25 al., 2012; Boutchko et al., 2012; Fernø et al., 2015; Gauteplas, 2015; Hoff et al., 1996).

Most of these geoscientific PET studies have been conducted with clinical scanners of cooperating medical departments. Typically, this limits the possibilities for hardware and software tuning, constrains the spatial resolution to 3 to 5 mm, impedes long term studies (longer than some hours), and application of proprietary software might distract from pushing forward the development of algorithms for enhanced image quality.

30 Our workgroup systematically developed and applied PET-scanners for geoscientific research in the course of over one decade (Richter and Gründig, 2000; Richter et al., 2005; Wolf et al., 2010; Gründig, 2002; Gründig et al., 2007; Kulenkampff et al., 2008; Kulenkampff et al., 2010; Barth et al., 2014a; Barth et al., 2014b; Kulenkampff et al., 2015; Kulenkampff et al., 2013b; Kulenkampff et al., 2013a). First published experiments were conducted with a self-constructed

PET-scanner for soil columns and rock cores, designed for slow transport studies (Richter and Gründig, 2000). We also applied clinical PET and PET/CT scanners, and since 2007 we use a high-resolution PET-scanner (ClearPET by Raytest, Germany), designed for biomedical research on animals (Sempere Roldan et al., 2007).

2 Methods

5 ### 2.1 Principle

PET responds to the emission of radiation caused by positron decay. A positron-emitting isotope is applied as radiotracer for labelling the substance which propagates through the sample during the observed process.

In order to compute the concentration c of a chemical species in one voxel we have to consider the decay law Eq. (1) with time t, decay time $T_{1/2}$ of the tracer, and number of decaying atoms N (Lieser, 2001)

$$N = \frac{N_0}{2^{\frac{t}{T_{1/2}}}} = N_0 \cdot \exp\left(-\frac{\ln 2 \cdot t}{T_{1/2}}\right). \tag{1}$$

With the activity A

$$A = \frac{dN}{dt} = \frac{\ln 2}{T_{1/2}} \cdot N \tag{2}$$

we can calculate the concentration of the decaying nuclide (with the voxel volume V) from the measured activity:

$$c = \frac{A \cdot T_{\frac{1}{2}}}{N_A \cdot V \cdot \ln 2}. \tag{3}$$

15 Often, the tracer isotope is used for labelling a carrier solution with the natural isotopic composition, in order to avoid specific interaction effects acting exclusively on the tracer. Then the concentration of the labelled carrier solution is determined by the fraction of tracer atoms in the carrier solution.

Positron-emitting isotopes exist of virtually all natural elements. However, only a small fraction of theses nuclides is producible with acceptable expenditure, and only a few nuclides are practically useful, because decay time, positron energy,
20 and other types of decay radiation have to be considered (Hawkesworth and Parker, 1995; Richter et al., 2005). We applied a number of GeoPET-isotopes, which are listed in Table 1.

PET makes use of the coincidence detection of the photon pair transmitted by the annihilation of the positron which occurs when a slowed-down positron interacts with an electron. The initial kinetic energy of the positron determines its free path length in matter. Therefore, the positron energy determines the fundamental limit of resolution, which is in the order of
25 1 mm in water and decreases with increasing electron density (Levin and Hoffman, 1999).

The annihilation radiation of the positron has the rest energy of an electron, 511 keV. Because of the minor energy resolution of PET-scanners, background radiation or portions of the γ-spectrum of the nuclide may interfere with the coincidence

detection. Particularly, γ-energies in excess of 1022 keV may produce positron–electron pairs anywhere in the material, with subsequent annihilation of the positron without relation to the tracer position ("false events"). These false events are correlated and remain unfiltered by the coincidence detection. This is in contrast to background radiation, single γ-quanta, which produce a background noise of random coincidences.

5 The radiation is usually detected in detector crystals that are mounted on multichannel photomultipliers. The detection-probability depends on the crystal parameters and is rather small and also strongly reduced by inevitable gaps between the crystals. Two events which are detected in opposite detector positions, within an energy window around 511 keV, e.g. 350–700 keV, and within a small coincidence window (typically 20 ns), are accepted as coincidences. This type of coincidence filtering is highly efficient, and only about 3% of the registered events are recorded as coincidences. Variation of the

10 coincidence window size provides an estimate of the random coincidences.

The geometrical parameters of the connecting line between the detection positions (line of response: LOR) are stored as projection files of "bins" from which the 3D tracer distribution is reconstructed. The total number of required coincidences for image reconstruction is typically in the order of 10^7, depending on the source distribution. Another algorithm allows fast particle tracking (PEPT) (Parker et al., 1993): When only a few distinct particles are labelled, their position can be

15 reconstructed from a small number, at least two linearly independent LORs.

Currently, the detector crystals of clinical PET-scanners are comparatively large, in order to optimize detection efficiency, which also accelerates the examination time and reduces the dose for the patient. As a consequence, these scanners do not accomplish the maximum spatial resolution (3–5 mm). This is the domain of biomedical PET-scanners with a smaller field of view (FOV) that are designed to achieve the maximum resolution (around 1 mm) (Cherry and Chatziioannou, 2004).

20 Generally, the number of coincidences, and thus the frame length, determines image quality. Typically, the maximum frame rate is in the order of minutes and depends on the quantity and distribution of activity in the FOV.

The sample material plays a minor role and eventually may be neglected when the density is low. In dense material, however, both attenuation and scattering should be considered, although interaction effects between 511-keV-photons and matter are low compared to the energy range of common μCT-sources (Fig. 1).

25 We have to assume a loss of photon radiation intensity I, which is described by the linear attenuation coefficient μ

$$\frac{dI}{dr} = -\mu \cdot I(r) \,. \tag{4}$$

In the energy range of annihilation photons the most probable interaction with matter is Compton scattering. The linear Compton attenuation coefficient μ_c is related to the Compton cross section σ_c by

$$\mu_c = \sigma_c \rho \frac{N_A \cdot Z}{A} = \sigma_c \cdot \rho_e \tag{5}$$

30 with the electron density ρ_e, which depends on bulk density ρ, mean atomic number Z, and mean atomic mass A of the material. The mass attenuation coefficients μ/ρ are material parameters in the range of 0.081–0.096 cm^2 g^{-1} (at 511 keV) and can be looked up in the XCOM database at NIST (Berger et al., 2010). Therefore, it is obvious that the main factor

controlling attenuation is density ρ. Attenuation coefficients of typical materials derived from this database are tabulated in Table 2. Therefore, in geological materials with a density above 2 g cm^{-3} we have to consider an attenuation of 80% through a sample with diameter of 10 cm.

Compton scattering means that photons are deflected from the straight LOR, simultaneously lose a portion of their energy

5   and eventually leave the energy window — which is considered as attenuation. The solid deflection angle θ is implicitly described by the Klein-Nishina formula

$$\frac{d\sigma_c}{d\Theta} = \pi r_e^2 \sin\Theta \cdot \frac{1+\cos^2\Theta}{\left(1+\alpha_e(1-\cos\Theta)\right)^2}\left(1 + \frac{\alpha_e^2(1-\cos\Theta)^2}{(1+\cos^2\Theta)\cdot\left(1+\alpha_e(1-\cos\Theta)\right)}\right) \tag{6}$$

with the classical electron radius r_e (2.818·10-15 m) and $\alpha_e = \frac{E_0}{m_e \cdot c^2} \leq 1$ (E_0: initial photon energy, $m_e c^2$: energy equivalent of the electron).

10   There is no simple way to apply this formula for scatter correction. A number of scatter correction algorithms are available (Zaidi, 2001; Zaidi and Montandon, 2007) which generally were developed for medical PET-applications, where the material density is low. We found that the application of simple algorithms based on some type of filtering of the projections or the resulting images are not appropriate in highly scattering material. More recent algorithms based on approximations of a scatter model are more suited. In order to evaluate such algorithms for dense material, we conducted Monte-Carlo

15   simulations with which all relevant reactions are considered and which allow tracing back the history of all events and differentiating and quantifying scattered and unscattered events (Zakhnini et al., 2013).

2.2 Specifications and requirements

A radioisotope laboratory is required that allows safe handling of activities and high local dose rates. Short living PET-

20   tracers have to be produced on-site with a cyclotron, like IBA cyclone 18/9 in our laboratory (Mansel et al., 2014; Mansel, 2015); longer living nuclides, like ^{22}Na, can be purchased.

Our ClearPET-scanner was optimized for geoscientific questions. It features a rotating gantry with 20 detector cassettes, each equipped with four 8·8-multichannel detectors and double-layered miniaturized detector crystals (LYSO/LuYAP, both 2·2·10 mm^3), in order to achieve a spatial resolution at the physical limit. The gantry diameter can be adjusted to 13.6 cm or

25   23.7 cm, allowing investigating samples with the typical dimensions of soil columns and drill cores. Its adjustable FOV has a maximum diameter of 160 mm and a length of 110 mm. Compared to medical PET-scanners we take advantage from higher resolution and sensitivity. In the case of ClearPET, this increase of sensitivity and resolution is achieved at the cost of less homogeneity of the field of view. This adverse effect for image quality is caused by inevitable gaps between the individual detector modules and somewhat mitigated by a rotating gantry.

Usually, frames with a length of 20–60 minutes are recorded and later subdivided or merged into frames of appropriate length. Process monitoring is then accomplished with sequential 3D-images with a minimum frame rate of 60 s, the gantry rotation period. The maximum observation period is limited by the decay of the radiotracer to about $8*T_{1/2}$.

Currently, the orientation of the gantry axis is horizontal; therefore a horizontal orientation of the samples is preferred. In near future the scanner will be upgraded with a tilting device to allow vertical orientation of the samples. A similar approach was taken by ClearPET-neuro (Weber et al., 2006).

Frequently the samples are formatted as cylinders and cast in epoxy with inlet and outlet ports at the end planes, which are connected with plastic fittings and tubing. The well-defined geometry facilitates the computation of the attenuation and scatter corrections. If pressure vessels are required, low density material should be used, like carbon fibre reinforced polymers (CFRP), aluminium or titanium. According to their Compton cross section, steel fittings or casings should be avoided or minimized. However, even with a point source in a steel pressure vessel with 5 mm thick walls we experienced satisfactory image quality.

2.3 Data processing

The original reconstruction and correction software is based upon the open-source STIR-library (Thielemans et al., 2012), amended with procedures provided by the manufacturer which are based on the work of Weber et al. (2006). We tuned these procedures in order to consider strong attenuation and scattering. Abundant data storage ("listmode-files" of single events) and the use of this open-source image reconstruction system eases adaptation to our particular requirements, but also exacerbate operating comfort.

The OSEM-reconstruction algorithm (Jacobson et al., 2000) implemented in STIR is an iterative procedure (iteration step j) for computing the activity a in one voxel v from the count number n in a set of bins b described by

$$a^{(j+1)}(v) = \frac{a^{(j)}(v)}{\sum_{B_k} p(v,b)} \sum_{B_k} \frac{p(v,b) \cdot n(b)}{\sum_V a^{(j)}(v') \cdot p(v',b)} \tag{7}$$

with the probability $p(v,b)$ that one coincidence originating from the voxel v in the 3D-volume space V is detected and assigned to the bin b in the 4D-projection space B, which is divided into subsets B_k. The detection probability matrix is composed of

- $p_n(b)$: efficiency of the detector pair attributed to b,
- $p_\rho(b)$: probability that the event is not attenuated in the medium, and
- $p_g(v,b)$: geometrical probability, according to

$$p(v,b) = p_g(v,b) \cdot p_n(b) \cdot p_\rho(b) . \tag{8}$$

The OSEM-algorithms is an accelerated version of the standard EM-algorithm (Shepp and Vardi, 1982) which divides the problem into m subsets with index k. When these subsets are balanced, i.e. the sensitivity image is independent of the subsets

$$p(v) = m \sum_{B_k} p(v, b) \, , \tag{9}$$

Eq. (7) reduces to

$$5 \quad a^{(j+1)}(v) = \frac{m \cdot a^{(j)}(v)}{p(v)} \sum_{B_k} \frac{p_g(v,b) \cdot n(b)}{\sum_V a^{(j)}(v') \cdot p_g(v',b)} \, , \tag{10}$$

which is implemented as OSEM-procedure in STIR.

Applying ClearPET, we have to consider mainly azimuthal gaps between the single detectors which, due to the rotating gantry, cause strip patterns of the projections (sinograms) (Fig. 2). This limits the validity of Eq. (9) to $m \leq 2$. The choice of two subsets still accelerates the reconstruction procedure with respect to the EM-algorithm ($m = 1$) and accords widely with

10   the condition Eq. (9).

The azimuthal gaps also cause strong variations of the sensitivity $p(v)$ in the denominator of Eq. (10), which reduces the robustness of the algorithm. We observed that errors are accumulated in in low sensitivity zones and destabilize the iteration process.

In order to calibrate the image $a(v)$ (activity a per voxel v) in concentration units, scalar factors for frame length, radioactive

15   decay, scanner dead time, and a calibration factor for the total sensitivity have to be applied. The dead time correction considers the efficiency decrease of the detectors with increasing activity and is implemented in the reconstruction algorithm as polygon fit of the count rate vs. activity curve. The decay correction should consider the frame length t_{fr}, when it is long with respect to the decay time $T_{1/2}$:

$$a_{corr} = a \cdot 2^{\frac{t_{img} - t_{exp}}{T_{1/2}}} \cdot \frac{t_{fr} \cdot \left(1 - 2^{-\frac{1}{T_{1/2}}}\right)}{1 - 2^{\frac{t_{fr}}{T_{1/2}}}} \, , \tag{11}$$

20   with the start time of the image (t_{img}) and experiment (t_{exp}), respectively.

The calibration of the total sensitivity could be computed with a pre-determined parameter from a calibrated phantom. This neglects the quantitative effects of the corrections and therefore is a rough estimation. A better method is the use of calibration sources together with the sample in the FOV, which are recommendable in any case as fiducial marks for later co-registration with other imaging modalities.

2.3.1 Reconstruction parameters and corrections

The effect of unequal detector efficiencies p_n is determined with normalization measurements on homogeneous phantoms; therefore, measuring errors have to be considered. A normalization tomogram is shown in Fig. 3. The noise level was

reduced considering symmetries. Also, we developed gap-filling strategies in order to reduce the impact of void bins in the projections. Nevertheless, we have to consider zones with low sensitivity, which are prone to higher error levels.

Another component of the sensitivity that has to be determined is attenuation p_ρ. In order to avoid additional noise from low-level measurements it is recommendable to compute it from a geometrical attenuation model. The LORs are compositions of

5   the pathways of the positron pair, therefore they traverse the complete sample, and attenuation is given by the projection of an attenuation image of the sample:

$$I_c = I_{c,0}e^{-\int_{R_1}^{R_2}\mu(r)dr} ,$$
(12)

with $I_{c,0}$ and I_c the source and recorded intensity, respectively, and the integration variable r running over the connecting line between both detectors at R_1 and R_2. The attenuation image $\mu(r)$ can be constructed geometrically or computed from a low-

10   resolution CT-image with estimates of the density and the mass attenuation coefficients, and the attenuation probability is

$$p_\rho(b) = e^{-\int_{R_1}^{R_2}\mu(r)dr} .$$
(13)

Scatter is considered as an additional process which adds coherent noise and therefore must be subtracted from the measured projections. We apply the single scatter simulation (SSS) algorithm from STIR 3.0 for correcting the scatter effect (Tsoumpas, 2004). This algorithm was verified (Zakhnini et al., 2013; Kulenkampff et al., 2016) for dense material with

15   Monte-Carlo (MC) simulations of the PET-measurements with OpenGATE (Jan et al., 2004), which quantitatively yield magnitude and distribution of all events. Estimated source distributions from MC-simulations were applied to compute the scatter fraction with which the SSS-results were scaled. This solves both the quantification issue of the SSS which is due to the large number of void bins outside the source distribution, and reduces the enormous computational effort for MC.

20   **2.4 Error estimation**

In contrast to CT, which commonly is segmented into a binary image, PET responds to the concentration of the propagating tracer as a continuous variable: Here, spatial resolution is the parameter of the response function which controls the smoothing of the image. More meaningful characteristics of PET images than spatial resolution are quantification errors, noise level, and the detection threshold.

25   A rigorous error analysis of the PET imaging procedure is an intricate task (Prekeges, 2013; Kirov, 2012; Meikle and Badawi, 2005). The analysis starts on the detector level. Although the total number of recorded events is large (e.g. 10^7), the matrix of projections is sparse, and the count numbers are stochastically responding to the Binomial distribution. The reconstruction procedure is a complicated surjective mapping method from the projection space of measurements to the image space, thus with a huge system matrix, which requires additional parameters (normalisation, attenuation correction,

scatter correction) that are also subject to errors. Currently, a strict error propagation analysis of this complex system is not feasible.

A rough error estimate can be calculated from the number of counts N that are projected onto one voxel. This number is large; therefore we can approximately consider the Poisson distribution with a relative error $\sigma = 1 / \sqrt{N}$. It is

5 typically in the order of ±10% or less and can be minimized by increasing activity or frame duration.

According to Strother et al. (1990) we can compute the signal to noise ratio (SNR) for each voxel from the weighted variance of all bins contributing to the particular voxel according to

$$SNR(v) \sim \left. tr(v) \middle/ \sqrt{Var(v)} \right. . \tag{14}$$

When the numbers of true tr, random rnd, and scattered sc counts for each bin are known, the variance term can be written as

10 backprojection of all these events

$$Var(v) = \sum_B p(v,b) \cdot (tr(b) + rnd(b) + sc(b)) . \tag{15}$$

With this variance term we can estimate the spatial distribution of the relative error σ' as

$$\sigma'(v) = \frac{\sqrt{\sum_B p(v,b) \cdot (tr(b) + rnd(b) + sc(b))}}{\sqrt{\sum_B p(v,b) \cdot tr(b)}} . \tag{16}$$

The expected value $tr(v)$ is the result of the iterative image reconstruction procedure, which applies normalization, and

15 therefore not equally scaled as the backprojection, which is not normalized. This is the reason why we refer to the backprojection of tr, not the iterative reconstruction.

However, we also have to consider systematic errors that are caused by deficiencies of the reconstruction algorithm and the parameter values. These are identifiable as imaging artefacts occurring in zones where the sensitivity, i.e. the magnitude of the response function of the mapping from the projections to the image, is low (small amplitudes in Fig. 3). Eventually, these

20 artefacts include zeros (e.g. from scatter-overcorrection) or large errors in the order of a factor 2.

In summary, the error depends on the number of counts per voxel and is typically in the order of 10%. In zones with lower sensitivity it eventually diverges and produces ring artefacts.

2.5 Detection threshold

25 Apart from the relative error we have to consider a detection threshold of activity below which the source is not reliably detected. This threshold depends on the background level, detector properties and the reconstruction procedure. The background coincidence count rate, as deduced from blank measurements, is in the order of 500 cps. However, scattered

events from strong sources can also be considered as background, in so far as they are not considered by the scatter correction procedure. A general threshold is caused by the number of events required to reconstruct one voxel. This threshold was determined with the help of Monte-Carlo simulations of ^{22}Na-point sources in Opalinus clay to be as low as 10 Bq/voxel, corresponding to a total of 50 counts in 18 minutes.

5   With decreasing activity the number of detected coincidences falls below a threshold where the source cannot be reconstructed. Practically, this threshold depends on many parameters and conditions, in particular noise level, sensitivity, reconstruction procedure, scatter and attenuation. We estimated the detection threshold with the help of a Monte-Carlo simulation of five point sources with diameter of 1 mm each, which were distributed along an axial profile in the Opalinus sample and one with a radial offset. Figure 4 is a reconstructed image of the initial situation, showing some scattering around

10 the four point sources.

The initial activity of 82 kBq was stepwise reduced by a factor two down to 1.2 Bq. The recording time was 18 min. It should be noted that the maximum count number per bin decreases from initially 81 to 1 at the seventh step (factor 64).

Figure 5 shows the peak amplitudes of the reconstructed image at the point source locations against the total activity of the sources. One peak disappears at the 14th step, representing a total activity of 50 Bq, or 10 Bq of the single point source. At

15 this point, the other sources are still detectable, but with a high quantification error, and strongly deviating from the proportionality line. Therefore, we define as best-case detection threshold the activity concentration of 10 Bq/voxel. Above this threshold the response is linear over at least 4 orders.

3 Examples

20 ### 3.1 Granite fracture (clinical scanner)

As an early example for the application of a clinical PET scanner, we review an experiment from Kulenkampff et al. (2008) which was conducted with a Siemens ECAT HR+ scanner in collaboration with the clinic and polyclinic for nuclear medicine of the Leipzig university hospital. It was conducted on a granitic drill core (diameter 5 cm, length 15 cm) with one large axial fracture, which originates from the Äspö HRL. The core was glued into a plastic cylinder and the fluid was

25 injected through grooves in the end pieces. A µCT-image by Enzmann and Kersten (2006) yields a mean aperture of the fracture of 0.5 mm with local enlargements up to 2 mm.

5 mL of a 0.01 M [^{18}F]KF solution was stepwise injected into the sample with a flow rate of 0.1 mL min^{-1}. Six frames with a length of 15 min were taken with the clinical scanner at stopped flow conditions.

Figure 6 shows the segmented fracture from the µCT and the propagation of the tracer cloud that was recorded with the PET-

30 scanner and reconstructed with the standard iterative 3D-reconstruction method of the scanner. The tracer cloud is displayed as transparent iso-surfaces, in order to show the intensity distribution.

The tracer distribution appears as smooth cloud which expands up to 1 cm in perpendicular direction from the fracture surface. This is due to the comparatively low spatial resolution of roughly 5 mm of this particular scanner and reconstruction method. However, it is obvious that the effective volume for the flow process is reduced to a preferential pathway along the fracture plane. A later experiment with a slower flow rate of 0.001 mL min^{-1} and with the longer living PET-nuclide [124]I

5   yielded some broadening of the flow pattern within the fracture plane. The spatial resolution was not sufficient to confirm dispersion of the tracer into the material adjacent to the fracture.

Practically, the conditions in a nuclear medical department are suitable for short-term experiments with short-living nuclides, as far as practicable with a mobile experimental setup. They are inappropriate for long-lasting procedures, specific analytical online techniques, and application of long-living radionuclides. Also, the non-transparent proprietary reconstruction software

10   could restrain adjustment to the conditions of strongly absorbing and scattering dense material. In our example, we had no control of the absorption and scatter correction procedure, which might have caused unnecessary blurring of the images. Consequently, since then we use a high-resolution scanner with which we produced the following examples.

3.2 Stassfurt sandstone (high-resolution scanner)

15   A complete sandstone drill core (diameter 100 mm) from the bunter sandstone in Staßfurt (NE-Germany) with a diagonal fracture system parallel to the bedding was cast in epoxy (Fig. 7). The fractures were sealed with adhesive tape to prevent entering of the resin. The core was cut at the inlet side in order to prepare a smooth surface at the inlet with a minimum gap space(<0.1 mm) between the sample and the end cap, because preceding experiments had shown that the active tracer in a large gap volume acts as persistent source impairing image quality by scattered radiation.

20   Saline formation water was prepared and flushed through the sample with a flow rate of 0.02 mL min^{-1} for 1 day. 5 mL of this carrier solution was labelled with 0.01 M [^{18}F]KF with an activity of 150 MBq and injected with the same flow rate. Then, after 250 min, unlabelled carrier solution was injected again. The experiment is reported in detail in Wolf (2010).

The input zone of the sample was positioned during and after the injection of the tracer pulse in the FOV of the PET-scanner. 38 frames were recorded during 10 h of continuous injection, with a frame length increasing from 4–30 min. The increasing

25   frame length accounts for the tracer decay.

In Fig. 8, the iso-surfaces at the 3%-maximum-value of six frames are shown. The frame time, length, and injected volume are given in Table 3.

The tracer propagation pattern appears to follow selected pathways across the fracture surface of the single fracture that is intersecting the sample cross section. These pathways are forming a complex network of diverging and recombining

30   patterns. At the zone where the pattern reaches the sample surface, 50 mm from the injection plane, the tracer disappears. This is both caused by the decay and the dispersion into a larger volume, because both effects reduce the activity concentration and thus decimate the number of counts per voxel below the noise level and the detection threshold.

The tomograms of Fig. 8 were produced with an enhanced version of the original reconstruction procedure. Corrections for random coincidences, dead-time, attenuation, scatter, and image normalisation were performed. In particular, the scatter correction strongly enhances image quality. The scattered radiation was determined with the STIR-SSS-algorithm. These scatter data were scaled to fit the scatter-fraction of 45%, which was estimated from Monte-Carlo simulations on similar material. As example, the impact of the scatter correction is shown in Fig. 9 as cross sections of frame 5 from Fig. 8. A spatial amplitude distribution of the same frame is given in Fig. 10.

The relative stochastic error is considered according to Eq. (16). The variance was calculated as backprojection of the uncorrected data, and the reference $tr(v)$ was estimated as the backprojection of the random- and scatter-corrected data. Figure 11 shows that the maximum error is 10% in the responsive regions where significant numbers of counts were recorded. It depends on the geometric sensitivity, which is considered as backprojection coefficient, and the total number of counts per voxel. The major portion of the stochastic error in these responsive regions is caused by scatter, while the typical random rate is about 1%. Outside of these regions the random rate, and thus the error and SNR, is due to background radiation, scattered events, and coinciding singles from different decay events. In adjacent zones to active regions the impact of scattering degrades the SNR and the detection threshold, respectively. Far from active regions, scattering becomes negligible, and the detection threshold only depends on the low random rate.

Figure 11 also shows the impact of less sensitive zones on the stochastic error. In these zones the total count rate is reduced, because they respond to a smaller number of projection bins, and therefore the error increases. Unfortunately, currently the OSMAPOSL-reconstruction algorithm preferentially projects inconsistent events (i.e. noise) into these less sensitive zones. This causes additional systematical errors which are recognizable as circular artefacts. Here, we could eliminate these artefacts to a large extent by optimizing the normalization data, although they are still perceptible in the cross sections of Fig. 9 as stripe patterns parallel to the axis.

3.3 Diffusion in Opalinus clay

Imaging with PET is a particularly convenient method when diffusion processes are considered where the only observable is concentration of a chemical species. We established PET as a quantitative method for observing spatially resolved diffusion patterns. From these patterns we derive anisotropic diffusion coefficients and information on heterogeneity on the scale of drill cores.

With measurements and Monte-Carlo model simulations we found that by its long decay time of 2.603 a and its well characterized chemical properties ^{22}Na is a particularly suited tracer for determining the material impact on tracer diffusion. The propagation velocity of the tracer front is in the order of 0.5–2 mm d^{-1} (Kulenkampff et al., 2016), which can be derived from the elliptical spreading of the of the tracer cloud (Fig. 12). Thus, this effect is hardly observable with clinical PET scanners with a resolution above 3 mm.

Anisotropic diffusion coefficients have been derived by an optimized finite element model (Lippmann-Pipke et al., 2016). These were in accordance with laboratory results of through-diffusion experiments. Departures from elliptical spreading are indications for heterogeneous effects that could be caused by fine layering.

4 Conclusions

5 GeoPET is proven to be applicable for tomographic process monitoring in geological materials. In fact, its molecular sensitivity, excellent selectivity for the decay of the particular radionuclide, and comparably high robustness with regard to material effects, we have to assign an outstanding rank for quantitative tomography of tracer transport, which is unrivalled by other tomographic modalities. The method should be applied when heterogeneous processes are considered.

It is highly recommendable to apply high-resolution scanners, like our ClearPET, because these provide the maximum
10 achievable spatial resolution and a higher sensitivity than large clinical scanners. This resolution in the order of 1 mm is the integration volume for the tracer concentration. It is a reasonable scale for process observations on the core scale, in the range of 10 cm, which also is the order of the representative elementary volume for a large group of inhomogeneous materials. The resolution of clinical PET-scanners (3–5 mm) is rather poor, compared to the maximum sample diameter of 10 cm, and tends to equilibrate the major features of inhomogeneous transport patterns.

15 However, high-resolution PET scanners afford more work expenses and are not yet mature technology. There is still need for further development, concerning reconstruction software, detection hardware, and the availability of tracers and labelling methods.

The progressing applications of geochemical simulations on the basis of pore-space models from μCT-images call for experimental verification. It appears that PET is the unique method which is capable to provide such data. Apart from that,
20 the examples demonstrate that it is able to deliver experimental process parameters (for example flow path distribution and flow velocity) that are hardly derivable with other methods and that are of fundamental relevance for reactive transport. The availability of such parameters offers prospects on realistic intermediate-scale model simulations of reactive transport which inherently incorporate the effects of conservative flow.

PET is the potential gold standard for geoscientific transport process tomography in laboratory studies, likewise to functional
25 PET-imaging in biomedical research and clinical applications. This is due to its unrivalled sensitivity for tracer concentrations in combination with an appropriate spatiotemporal resolution and immunity to matrix effects. These benefits are at the cost of high expenses and some limitations with respect to available tracers and labelling methods.

Acknowledgements. This work was partially financed by the Federal Ministry of Education and Research (grant no.
30 02C1536), the Federal Ministry for Economic Affairs and Energy (grant no. 02E10176 and 02E10971) and the European Atomic Energy Community Seventh Framework Programme (grant no. 516514, IP FUNMIG). The authors thank the Project Management Agency Karlsruhe (Water Technology and Waste Management Division) for project administration. We also

thank the Clinic and Polyclinic of Nuclear Medicine of Leipzig University and the Research Group Hydrogeochemistry of the Johannes-Gutenberg-University Mainz for cooperation.

References

Barth, T., Kulenkampff, J., Bras, S., Gründig, M., Lippmann-Pipke, J., and Hampel, U.: Positron emission tomography in
5 pebble beds. Part 2: Graphite particle deposition and resuspension, Nuclear Engineering and Design, 267, 227-237, http://dx.doi.org/10.1016/j.nucengdes.2013.07.015, 2014a.

Barth, T., Ludwig, M., Kulenkampff, J., Gründig, M., Franke, K., Lippmann-Pipke, J., and Hampel, U.: Positron emission tomography in pebble beds. Part 1: Liquid particle deposition, Nuclear Engineering and Design, 267, 218-226, http://dx.doi.org/10.1016/j.nucengdes.2013.03.011, 2014b.

10 Bendriem, B., and Townsend, D. W.: The theory and practice of 3D PET, Developments in Nuclear Medicine, 32, edited by: Cox, P. H., Kluwer Academic Publishers, Dordrecht, 1998.

Benton, D. M., and Parker, D. J.: Non-medical applications of positron emission tomography, in: Non-Invasive Monitoring of Multiphase Flows, edited by: Chaouki, J., Larachi, F., and Dudukovic, M. P., Elsevier Science B.V., 161-184, 1996.

Berger, M.J., Hubbell, J.H., Seltzer, S.M., Chang, J., Coursey, J.S., Sukumar, R., Zucker, D.S., Olsen, K.: XCOM: Photon
15 Cross Sections Database (NIST Standard Reference Database 8 (XGAM)): http://www.nist.gov/pml/data/xcom/, 2010.

Boutchko, R., Rayz, V. L., Vandehey, N. T., O'Neil, J. P., Budinger, T. F., Nico, P. S., Druhan, J. L., Saloner, D. A., Gullberg, G. T., and Moses, W. W.: Imaging and modeling of flow in porous media using clinical nuclear emission tomography systems and computational fluid dynamics, Journal of Applied Geophysics, 76, 74-81, http://dx.doi.org/10.1016/j.jappgeo.2011.10.003, 2012.

20 Cherry, S. R., and Chatziioannou, A. F.: Small Animal PET Systems, in: Emission Tomography, edited by: Wernick, M. N., and Aarsvold, J. N., Elsevier, San Diego/London, 213-228, 2004.

Degueldre, C., Pleinert, H., Maguire, P., Lehman, E., Missimer, J., Hammer, J., Leenders, K., Bock, H., and Townsend, D.: Porosity and pathway determination in crystalline rock by positron emission tomography and neutron radiography, Earth and Planetary Science Letters, 140, 213-225, 1996.

25 Enzmann, F., and Kersten, M.: X-ray computed micro tomography (μ-CT) results of a granitic drill core, 1st annual workshop 6th EC FP - FUNMIG IP, Saclay, 2006.

Fernø, M. A., Gauteplass, J., Hauge, L. P., Abell, G. E., Adamsen, T. C. H., and Graue, A.: Combined positron emission tomography and computed tomography to visualize and quantify fluid flow in sedimentary rocks, Water Resources Research, 51, 7811-7819, 10.1002/2015wr017130, 2015.

30 Garrett, A. B.: Radioactive Tracers: George de Hevesy, Journal of Chemical Education 40, 36-37, 1963.

Gauteplas, J.: Pore-to-core Laboratory Upscaling and Visualization of Enhanced Oil Recovery and CO2 Storage, Dr., University of Bergen, Bergen, 2015.

Goethals, P., Volkaert, A., Jacobs, P., Roels, S., and Carmeliet, J.: Comparison of Positron Emission Tomography and X-ray radiography for studies of physical processes in sandstone, Engineering Geology, 103, 134-138, 2009.

Gründig, M., Richter, M., Seese, A., and Sabri, O.: Tomographic radiotracer studies of the spatial distribution of heterogeneous geochemical transport processes, Applied Geochemistry, 22, 2334–2343, 2007.

Gründig, M., Richter, M., Seese, A.: Positron emission tomography (PET) for investigation of water flow in soil columns, in: Geochemical Processes in Soil and Groundwater, edited by: Schuklz, H. D., Hadeler, A., Wiley-VCH, Weinheim, 549 - 559, 2002.

Hawkesworth, M. R., Parker, D. J., Fowles, P., Crilly, J. F., Jefferies, N. L., and Jonkers, G.: Nonmedical applications of a positron camera, Nuclear Instruments and Methods in Physics Research Section A: Accelerators, Spectrometers, Detectors and Associated Equipment, 310, 423-434, 1991.

Hawkesworth, M. R., and Parker, D. J.: Chapter 12 - Emission tomography, in: Process Tomography, edited by: Williams, R. A., and Beck, M. S., Butterworth-Heinemann, Oxford, 199-223, 1995.

Hevesy, G. V., and Paneth, F.: Die Löslichkeit des Bleisulfids und Bleichromats, Zeitschrift für anorganische Chemie, 82, 323-328, 10.1002/zaac.19130820125, 1913.

Hoff, W. D., Wilson, M. A., Benton, D. M., Hawkesworth, M. R., Parker, D. J., and Flowles, P.: The use of positron emission tomography to monitor unsaturated water flow within porous construction materials, Journal of Materials Science Letters, 15, 1101-1104, 10.1007/bf00539949, 1996.

Jacobson, M., Levkovitz, R., Ben-Tal, A., Thielemans, K., Spinks, T., Belluzzo, D., Pagani, E., Bettinardi, V., Gilardi, M. C., Zverovic, A., and Mitra, G.: Enhanced 3D PET OSEM reconstruction using inter-update Metz filtering*, Physics in Medicine and Biology, 45, 2417-2439, 2000.

Jan, S., Santin, G., Strul, D., Staelens, S., Assie, K., Autret, D., Avner, S., Barbier, R., Bardies, M., Bloomfield, P. M., Brasse, D., Breton, V., Bruyndonckx, P., Buvat, I., Chatziioannou, A. F., Choi, Y., Chung, Y. H., Comtat, C., Donnarieix, D., Ferrer, L., Glick, S. J., Groiselle, C. J., Guez, D., Honore, P. F., Kerhoas-Cavata, S., Kirov, A. S., Kohli, V., Koole, M., Krieguer, M., Laan, D. J. v. d., Lamare, F., Largeron, G., Lartizien, C., Lazaro, D., Maas, M. C., Maigne, L., Mayet, F., Melot, F., Merheb, C., Pennacchio, E., Perez, J., Pietrzyk, U., Rannou, F. R., Rey, M., Schaart, D. R., Schmidtlein, C. R., Simon, L., Song, T. Y., Vieira, J. M., Visvikis, D., Walle, R. V. d., Wieers, E., and Morel, C.: GATE: a simulation toolkit for PET and SPECT, Physics in Medicine and Biology, 49, 4543-4561, 2004.

Khalili, A., Basu, A. J., and Pietrzyk, U.: Flow visualization in porous media via Positron Emission Tomography, Physics of Fluids, 10, 1031-1033, 1998.

Kinsella, K., Schlyer Dj Fau - Fowler, J. S., Fowler Js Fau - Martinez, R. J., Martinez Rj Fau - Sobecky, P. A., and Sobecky, P. A.: Evaluation of positron emission tomography as a method to visualize subsurface microbial processes,

Kirov, A. S. S., C. Ross; Kang, Hyejoo; Lee, Nancy Rationale, Instrumental Accuracy, and Challenges of PET Quantification for Tumor Segmentation in Radiation Treatment Planning, in: Positron Emission Tomography - Current Clinical and Research Aspects, edited by: Hsieh, C.-H., InTech, 2012.

Kulenkampff, J., Gründig, M., Richter, M., and Enzmann, F.: Evaluation of positron-emission-tomography for visualisation of migration processes in geomaterials, Physics and Chemistry of the Earth, Parts A/B/C, 33, 937-942, http://dx.doi.org/10.1016/j.pce.2008.05.005, 2008.

Kulenkampff, J., Gründig, M., Zakhnini, A., Gerasch, R., and Lippmann-Pipke, J.: Process tomography of diffusion, using
5   PET, to evaluate anisotropy and heterogeneity, Clay Minerals, 50, 369-375, 10.1180/claymin.2015.050.3.09, 2015.

Kulenkampff, J., Gründig, M., Lippman-Pipke, J., and Zakhnini, A.: Quantitative experimental monitoring of molecular diffusion in clay with positron emission tomography, Solid Earth, this issue, 2016.

Levin, C. S., and Hoffman, E. J.: Calculation of positron range and its effect on the fundamental limit of positron emission tomography system spatial resolution, Physics in Medicine and Biology, 44, 781-799, 1999.

10 Lieser, K. H.: Nuclear and Radiochemistry, Wiley-VCH, Weinheim, 2001.

Mansel, A. F., K.: Production of no-carrier-added 135La at an 18 MeV cyclotron and its purification for investigations at a concentration range down to 10–15 mol / L, Radiochim. Acta, 103, 759-763, 10.1515/ract-2015-2427, 2015.

Meikle, S., and Badawi, R.: Quantitative Techniques in PET, in: Positron Emission Tomography, edited by: Bailey, D., Townsend, D., Valk, P., and Maisey, M., Springer London, 93-126, 2005.

15 Nagra: Technischer Bericht 02-03. Projekt Opalinuston. Synthese der geowissenschaftlichen Untersuchungsergebnisse, 2002.

Ogilvie, S. R., Orribo, J. M., and Glover, P. W. J.: The influence of deformation bands upon fluid flow using profile permeametry and positron emission tomography, GEOPHYSICAL RESEARCH LETTERS, 28, 61-64, 10.1029/2000gl008507, 2001.

20 Parker, D. J., Broadbent, C. J., Fowles, P., Hawkesworth, M. R., and McNeil, P.: Positron emission particle tracking - a technique for studying flow within engineering equipment, Nuclear Instruments and Methods in Physics Research Section A: Accelerators, Spectrometers, Detectors and Associated Equipment, 326, 592-607, 1993.

Parker, D. J., Hawkesworth, M. R., Broadbent, C. J., Fowles, P., Fryer, T. D., and McNeil, P. A.: Industrial positron-based imaging: Principles and applications, Nuclear Instruments and Methods in Physics Research Section A: Accelerators,
25 Spectrometers, Detectors and Associated Equipment, 348, 583-592, 1994.

Parker, D. J., Forster, R. N., Fowles, P., and Takhar, P. S.: Positron emission particle tracking using the new Birmingham positron camera, Nuclear Instruments and Methods in Physics Research Section A: Accelerators, Spectrometers, Detectors and Associated Equipment, 477, 540-545, 2002.

Phelps, M. E.: PET, Physics, Instrumentation, and Scanners, Springer, 2006.

30 Prekeges, J.: Nuclear medicine instrumentation, Jones & Bartlett Learning, Burlington, USA, 2013.

Richter, M., and Gründig, M.: Positron emission tomography for studies of water flow in soil columns, in: Applied mineralogy in research, economy, technology, ecology and culture; proceedings of the Sixth International Congress on Applied Mineralogy ICAM 2000, Göttingen, Germany, 17 - 19 july 2000 edited by: Rammlmaier, D., Balkema, Rotterdam, Rotterdam, 2000.

Richter, M., Gründig, M., Zieger, K., Seese, A., and Sabri, O.: Positron emission tomography for modelling of geochemical transport processes in clay, Radiochimica Acta, 93, 643-651, 2005.

Sempere Roldan, P., Chereul, E., Dietzel, O., Magnier, L., Pautrot, C., Rbah, L., Sappey-Marinier, D., Wagner, A., Zimmer, L., Janier, M., Tarazona, V., and Dietzel, G.: Raytest ClearPET(TM), a new generation small animal PET scanner, Nuclear Instruments and Methods in Physics Research Section A: Accelerators, Spectrometers, Detectors and Associated Equipment, 571, 498-501, 2007.

Shepp, L. A., and Vardi, Y.: Maximum Likelihood Reconstruction for Emission Tomography, Medical Imaging, IEEE Transactions on, 1, 113-122, 10.1109/tmi.1982.4307558, 1982.

Stein, M., Martin, T. W., Seville, J. P. K., McNeil, P. A., and Parker, D. J.: Positron emission particle tracking: Particle velocities in gas fluidised beds, mixers and other applications, in: Non-Invasive Monitoring of Multiphase Flows, edited by: Chaouki, J., Larachi, F., and Dudukovic, M. P., Elsevier Science B.V., 309-333, 1997.

Strother, S. C., Casey, M. E., and Hoffman, E. J.: Measuring PET scanner sensitivity: relating countrates to image signal-to-noise ratios using noise equivalents counts, Nuclear Science, IEEE Transactions on, 37, 783-788, 10.1109/23.106715, 1990.

Tenchine, S., and Gouze, P.: Density contrast effects on tracer dispersion in variable aperture fractures, Advances in Water Resources, 28, 273-289, http://dx.doi.org/10.1016/j.advwatres.2004.10.009, 2005.

Ter-Pogossian, M. M., Phelps, M. E., Hoffman, E. J., and Mullani, N. A.: A Positron-Emission Transaxial Tomograph for Nuclear Imaging (PETT), Radiology, 114, 89-98, 10.1148/114.1.89, 1975.

Thielemans, K., Tsoumpas, C., Mustafovic, S., Beisel, T., Aguiar, P., Dikaios, N., and Jacobson, M. W.: STIR: software for tomographic image reconstruction release 2, Physics in Medicine and Biology, 57, 867-883, 2012.

Tsoumpas, C. A. P. T. K.: Implementation and Evaluation of the Single Scatter Simulation Allgorithm in the STIR Library, MIC, 2004.

van den Bergen, E. A. J., G.; Strijckmans, K.; Goethals, P.: Industrial Applications of Positron Emission Computed Tomography, Nuclear Geophysics, 3, 407-418, 1989.

Wang, M.: Industrial Tomography, Woodhead Publishing Series in Electronic and Optical Materials, 71, Woodhead Publishing, Cambridge (UK), 2015.

Weber, S., Morel, C., Simon, L., Krieguer, M., Rey, M., Gundlich, B., and Khodaverdi, M.: Image reconstruction for the ClearPET(TM) Neuro, Nuclear Instruments and Methods in Physics Research Section A: Accelerators, Spectrometers, Detectors and Associated Equipment, 569, 381-385, 2006.

Weissleder, R., Ross, B.D., Rehemtulla, A., Gambhir, S.S.: Molecular Imaging, People's Medical Publishing House, Shelton, USA, 2010.

Wernick, M. N., and Aarsvold, J. N.: Emission tomography - The fundamentals of ÜPET and SPECT, Elsevier, San Diego/London, 2004.

Williams, R. A. B., M. S.: Process tomography:principles, techniques, and applications, Butterworth-Heinemann Ltd, Oxford (UK), 1995.

Wolf, M.: Visualisierung und Quantifzierung der Fluiddynamik in Bohrkernen aus dem Salinar und Deckgebirge des Raumes Stassfurt mittels Positronen-Emissions-Tomographie, Thesis, Fakultät für Physik und Geowissenschaften, Leipzig University, Leipzig, 121 pp., 2010.

Zaidi, H.: Scatter modelling and correction strategies in fully 3-D PET, Nuclear Medicine Communications:, 22, 1181-1184,

5   2001.

Zaidi, H., and Montandon, M.-L.: Scatter Compensation Techniques in PET, PET Clinics, 2, 219-234, 2007.

Zakhnini, A., Kulenkampff, J., Sauerzapf, S., Pietrzyk, U., and Lippmann-Pipke, J.: Monte Carlo simulations of GeoPET experiments: 3D images of tracer distributions (18F, 124I and 58Co) in Opalinus Clay, anhydrite and quartz, Computers & Geosciences, 57, 183-196, 10.1016/cageo.2013.03.023, 2013.
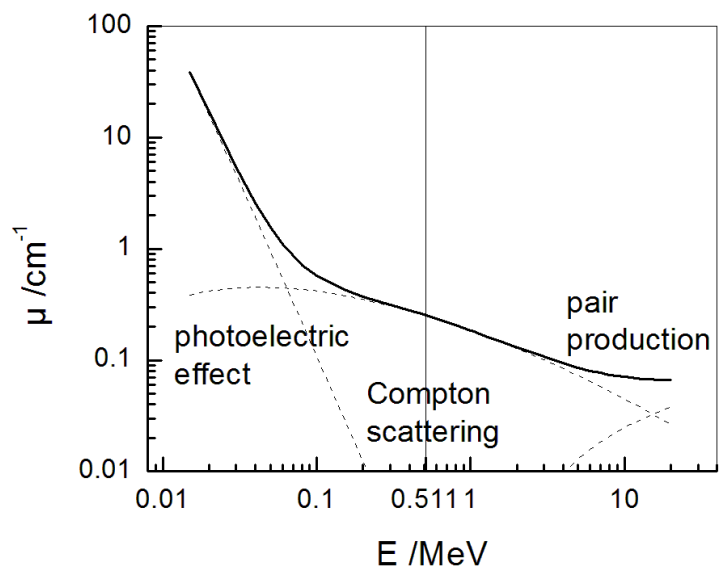
Figures

Figure 1. Linear attenuation coefficient μ of anhydrite, calculated with data from XCOM (Berger et al., 2010). The effective absorption process at 511 keV is Compton scattering.
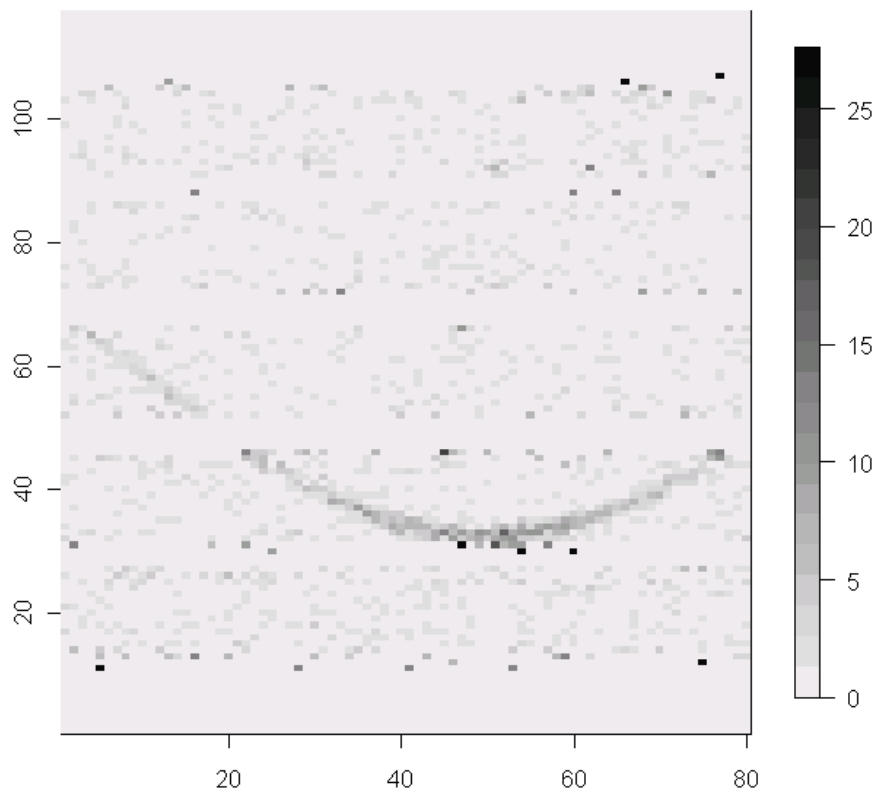
Figure 2. One typical sonogram of ClearPET (count number vs. radial and azimuthal coordinate), showing gaps between the detectors.
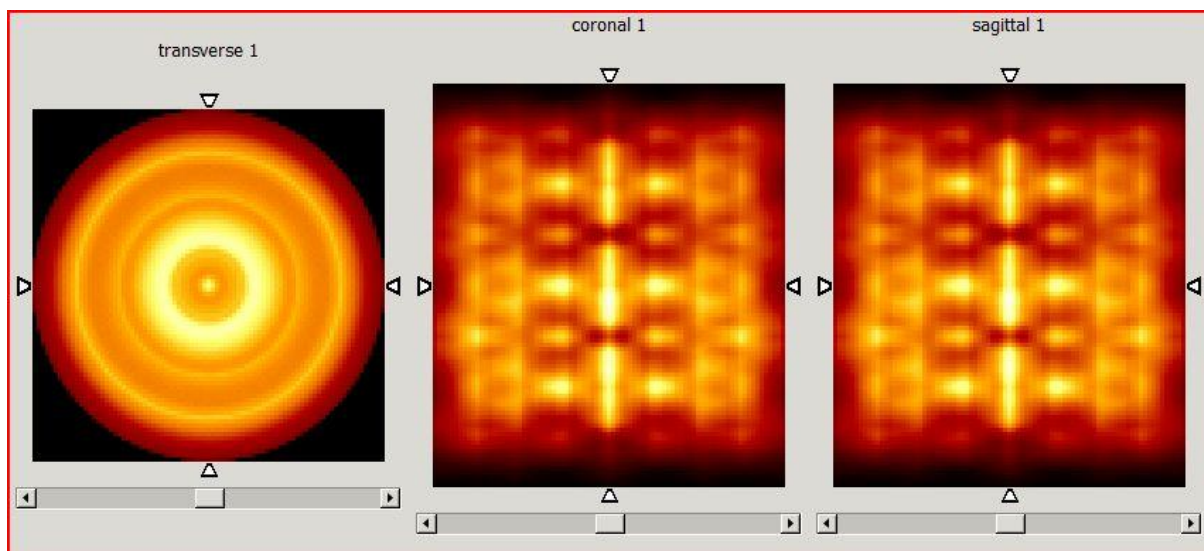
Figure 3. Normalisation tomogram of ClearPET: Backprojection of the measurement of a homogeneous cylinder source.
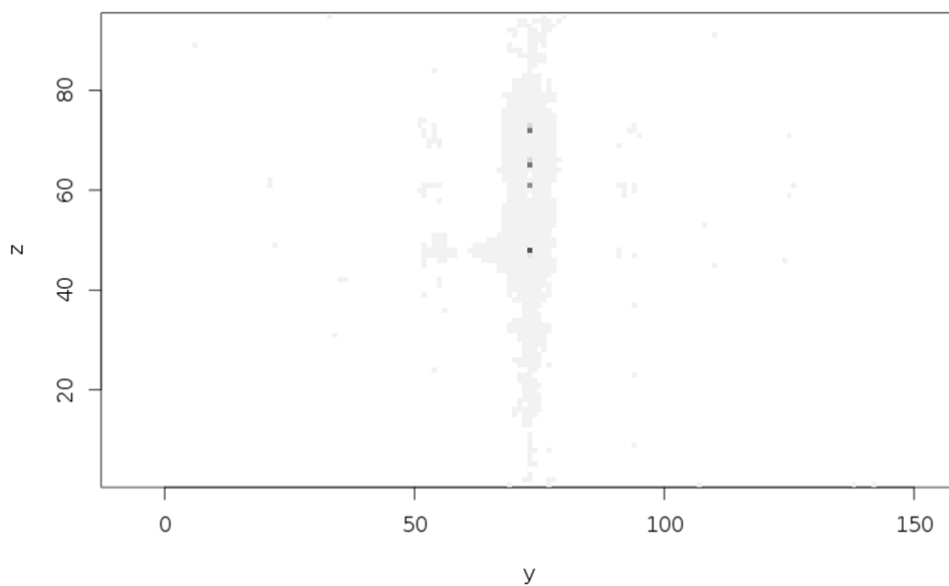
Figure 4. Reconstructed image of the Monte-Carlo simulation of four point sources in Opalinus clay material.
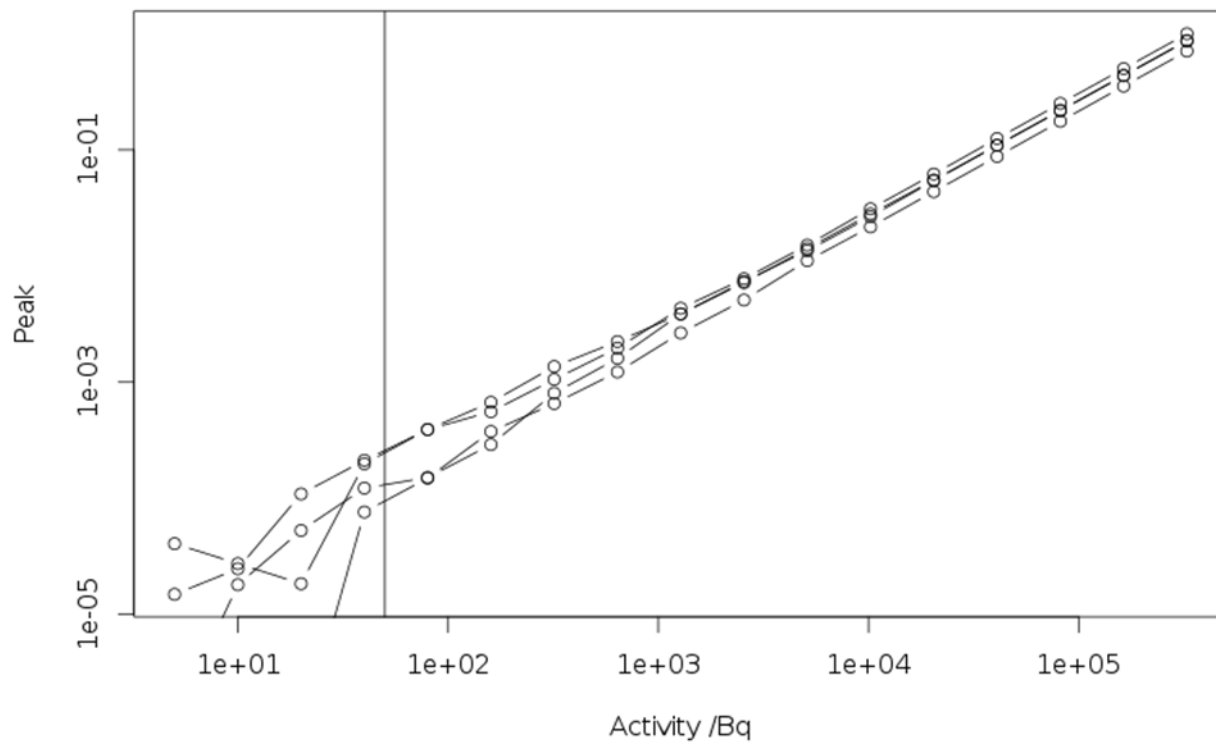
Figure 5. Peak amplitudes of the four point sources in Figure in dependence of the total activity.
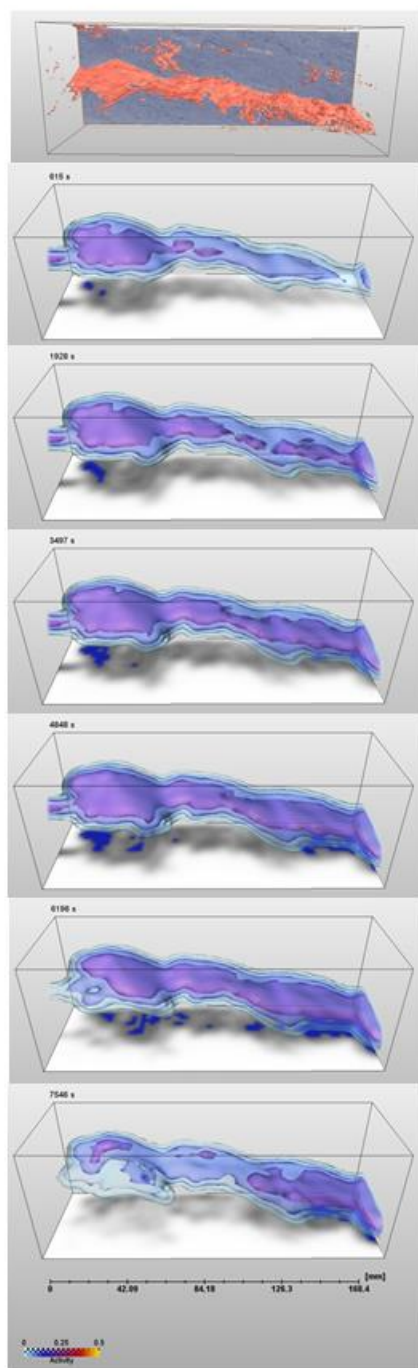
Figure 6. Top: μCT-image of a granite core with a single fracture (recorded at the Federal Institute for Material Research and Testing BAM, Berlin, and processed by F. Enzmann, Johannes-Gutenberg-University, Mainz). Below: 6 PET frames recorded with a clinical PET-scanner at clinic and polyclinic for nuclear medicine of the Leipzig university hospital.

Figure 7. Bunter sandstone drill core. Adhesive tape, preventing intrusion of the resin, is indicating the direction of the fractures
5   **(image taken from Wolf, 2010).**
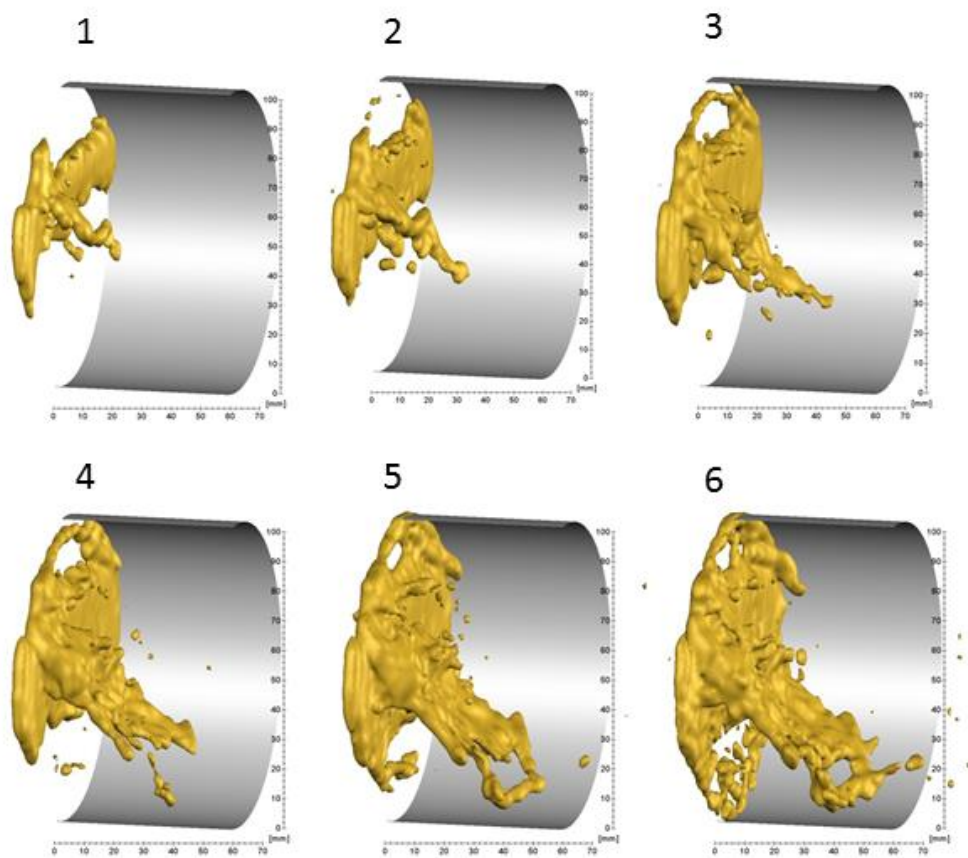
Figure 8. Result of the measurements with ClearPET during advection experiments on the sample in Fig. 6: Isosurfaces of the 3%-maximum-value for six frames (see Table 3).
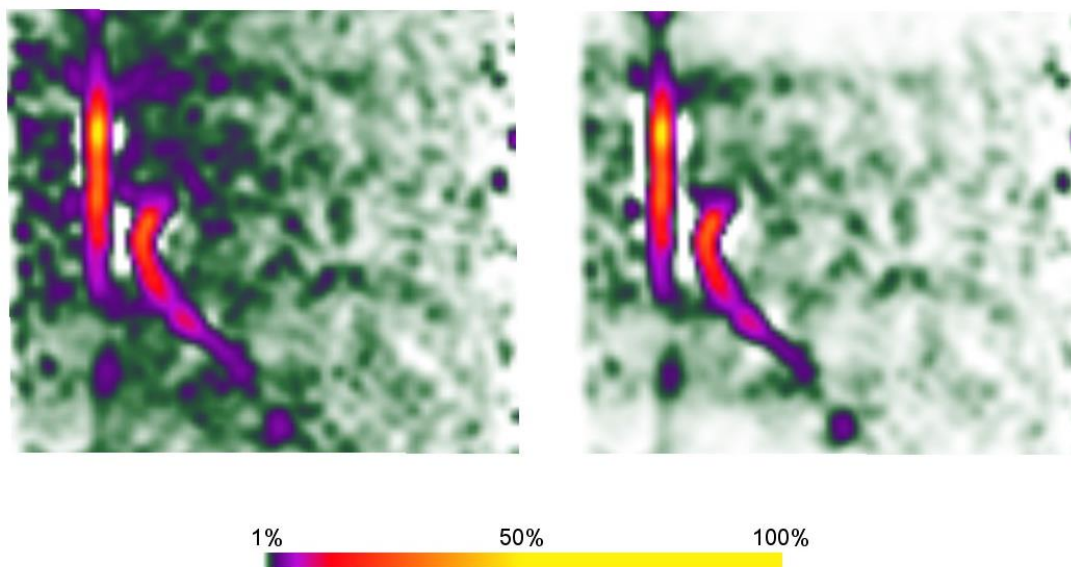
Figure 9. Vertical slice through frame 5 from Figure , left: without, right: with scatter correction. The color scale refers to the maximum value of the tomogram.
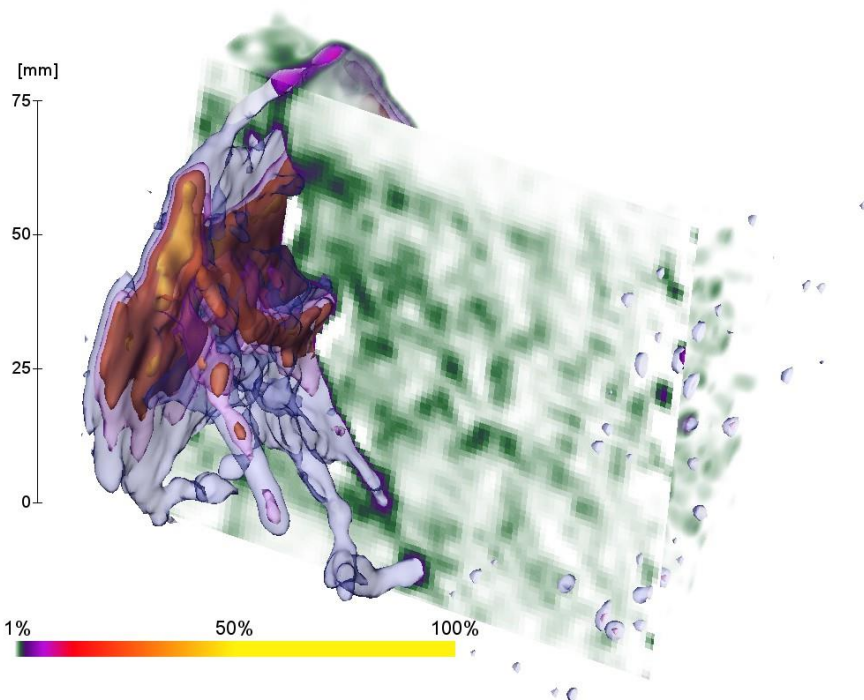
5   **Figure 10. Frame 5 from Figure with vertical slice from Figure and isosurfaces at 50%, 20%, 10%, 5%, and 2% of the maximum value**
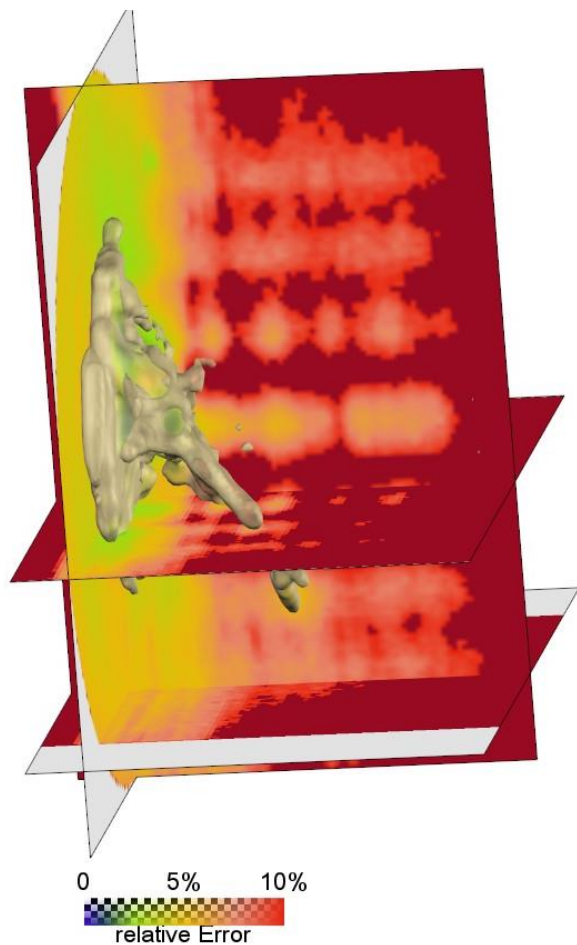
Figure 2. Sections of the relative stochastic error according to Eq. 16, and isosurface of the 3%-maximum-value, computed for frame 5 of Figure .
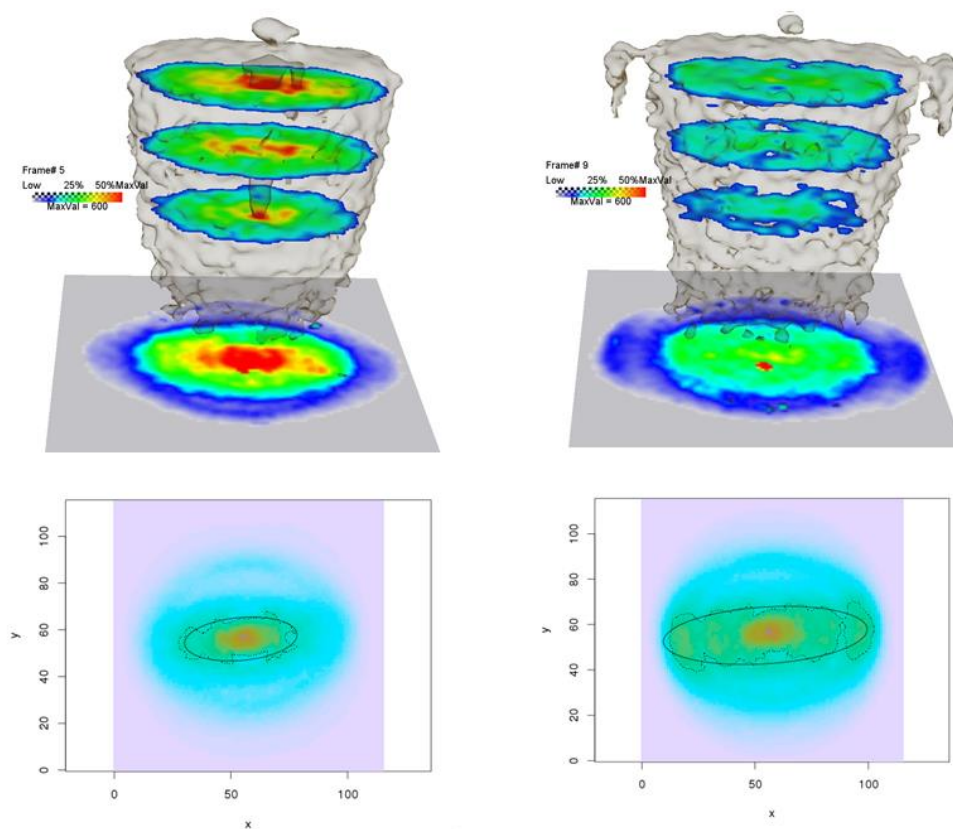
Figure 3. Top: Horizontal slices and axial projection of the tracer concentration tomograms during diffusion of ^{22}Na into Opalinus clay, after 13 and 27 days. Bottom: Axial projections with fitted FWHM-ellipsoids (full width half maximum). Deviations from the elliptical shape are indicating heterogeneous effects that are not considered as homogeneous anisotropy (Kulenkampff et al., 2016).

Table 1. Choice of PET-nuclides (data National Nuclear Data Center, information extracted from the NuDat 2 database, http://www.nndc.bnl.gov/nudat2/, 2016)

nuclide	$T_{1/2}$	$I(\beta+)$	$E_{mean}(\beta+)$	$E, I(\gamma)$
			keV	keV
^{18}F	109.77 m	96.7%	249.8	-
^{22}Na	2.6018 a	90.4%	215.9	1274.5/100%
^{45}Ti	184.8 m	84.8%	439	<1%
^{56}Co	77.24 d	19.7%	610	846.8/100%, 1038/14%, 1238/66%,1771/15%, 2598/17%
^{64}Cu	12.701 h	17.6%	278	<1%
^{86}Y	14.74 h	31.9%	660	443/17%, 628/33%, 703/15%, 777/22%, 1076/83%, 1153/31%, 1854/17%, 1920/21%
^{124}I	4.176 d	22.7%	820	603/63%, 722/10%, 1691/11%

Table 2. Attenuation properties at 511 keV of relevant materials (µ/ρ: mass attenuation coefficient, ρ: density, µ: linear attenuation coefficient, q: intensity through material thickness of 5 cm). Data assembled from the XCOM-database (Berger et al., 2010)

material	µ/ρ	ρ	µ	q (L = 5 cm)
	cm²/g	g/cm³	1/cm	%
water	0.0960	1.00	0.096	62%
saturated salt water	0.0927	1.20	0.111	57%
quartz	0.0866	2.65	0.229	32%
halite	0.0834	2.10	0.175	42%
crystalline rock	0.0862	2.80	0.241	30%
sandstone (20%)	0.0874	2.32	0.203	36%
anhydrite	0.0870	2.90	0.252	28%
Opalinus clay	0.0903	2.45	0.221	33%
PVC	0.0890	1.45	0.129	52%
PMMA	0.0932	1.19	0.111	57%
stainless steel	0.0835	7.98	0.666	4%
aluminum	0.0837	2.7	0.226	32%
lead	0.156	11.3	1.76	0.01%

Table 3. Injection parameters of Figure .

	1	2	3	4	5	6
t /min	95	155	215	325	405	615
l /min	6	6	6	10	18	30
Vinj /ml	1.9	3.1	4.3	6.5	8.1	12.3
Vcarrier /ml	0	0	0	1.5	3.1	7.3